Journal of Renewable and Sustainable Energy ARTICLE pubs.aip.org/aip/rse

Characterization of wind speed and directional shear at the AWAKEN field campaign site

Cite as: J. Renewable Sustainable Energy **15**, 033308 (2023); doi: 10.1063/5.0139737
Submitted: 22 December 2022 · Accepted: 11 April 2023 ·
Published Online: 20 June 2023

Mithu Debnath,[1,2,a)] Patrick Moriarty,[1] Raghavendra Krishnamurthy,[3] Nicola Bodini,[1] Rob Newsom,[3] Eliot Quon,[1] Julie K. Lundquist,[1,4] Stefano Letizia,[1] Giacomo Valerio Iungo,[5] and Petra Klein[6]

AFFILIATIONS

[1]National Renewable Energy Laboratory, Golden, Colorado 80401, USA
[2]AES Clean Energy, Louisville, Colorado 80027, USA
[3]Pacific Northwest National Laboratory, Richland, Washington 99354, USA
[4]University of Colorado at Boulder, Boulder, Colorado 80309, USA
[5]Department of Mechanical Engineering, The University of Texas at Dallas, Dallas, Texas 75080, USA
[6]College of Atmospheric and Geographic Sciences, and School of Meteorology, University of Oklahoma, Norman, Oklahoma 73019, USA

Note: This article is part of the special issue Preparatory Work for the American Wake Experiment (AWAKEN).
[a)]**Author to whom correspondence should be addressed:** mithu.debnath@aes.com

ABSTRACT

The American wake experiment (AWAKEN) is taking place in northern Oklahoma, USA, close to the Atmospheric Radiation Measurement Southern Great Plains (ARM SGP) atmospheric observatory. The planning for the deployment of the instruments in this observational field campaign required an assessment of the wind characteristics of the site. This paper analyzes long-term data collected by instruments at the ARM SGP observatory to characterize the winds near the AWAKEN site. The analysis shows that this site experiences high wind shear and veer events with a large number of nocturnal low-level jets. A total of 7086 low-level jet wind profiles over 6 years are examined and found to be dominant from the south and southeast. Significant nocturnal wind veer is observed, which causes southerly wind near the surface to become westerly wind aloft. By identifying a strong relationship between atmospheric stability and wind shear, the wind shear at the site is predicted using the Monin–Obukhov similarity theory (MOST) and validated with the observational data collected by a scanning Doppler lidar. The results show that wind speed at a height of 91 m, a proxy hub height for wind turbines in this area, can be predicted from data collected at a height of 10 m with a bias of −0.35 and 0.65 m s^{-1} in unstable and stable atmospheric boundary layers, respectively. The bias of the predicted wind speed is mostly in the region of low wind speed, and wind speed above 5 m s^{-1} at a height of 91 m can be predicted with a bias of less than 0.2 m s^{-1}, and the limitations of the MOST in predicting winds during the stably stratified boundary layer is well-observed.

I. INTRODUCTION

Observations collected from field campaigns are essential for understanding the variability of the atmospheric boundary layer (ABL) and improving numerical models. The American wake experiment (AWAKEN) field campaign,[1,2] funded by the U.S. Department of Energy (DOE), will characterize the interaction between wind power plants and the ABL, with a specific focus on wind turbine and wind plant wake effects and wind plant blockage. The field campaign will take place in northern Oklahoma, around the DOE's Atmospheric Radiation Measurement (ARM) Southern Great Plains (SGP) long-term atmospheric observatory. The instrumentation at the SGP allows for detailed characterization of wind conditions in the area, which is essential information for the field instrument placement and operation, tailoring the scientific objectives based on local conditions, and validating numerical models used to prepare for the experiment.

An accurate characterization of the wind regime at a site of interest not only requires an assessment of the mean wind speed at hub height but also a detailed analysis of wind shear and veer. In fact, the power extracted by a wind turbine depends on the available power flux through the rotor-swept area; the power flux is a function of the wind shear.[3,4] The rotors of modern utility-scale wind turbines span up to 250 m above ground level (AGL), so turbines will encounter

large variations in wind speed over the rotor layer.[5,6] Wind veer also has a direct impact on wind turbines, as changes in wind direction with height increase the loads on the turbine blades and impact power performance.[4,7] The change of wind shear and veer is primarily caused by atmospheric stability at a site,[8] with the strongest wind shear and strongest wind veer occurring in stably stratified conditions. Therefore, an accurate assessment of site-specific atmospheric conditions and stability is necessary to properly determine how different atmospheric conditions affect wind plant performance.

Each wind plant site is impacted differently by local surface roughness, radiative cooling and heating of the surface, moisture, and synoptic and microscale forcings. The AWAKEN field campaign[1] targets a region in northern Oklahoma, where the gradual west-to-east terrain slope can create a horizontal temperature gradient on a daily basis.[9] The thermal wind diurnally reverses direction in the lower atmospheric levels just above the surface. If the large-scale winds are southerly, as they frequently are in that region due to the pressure trough commonly found in the lee of the Rocky Mountains, this reversal increases near-surface winds at night and decreases them during the day. The wind can be highly ageostrophic, and the maximum wind speed is reached shortly after midnight[10] at the SGP site due to the inertial oscillations.[11] Bonner[12] used data from 47 radiosonde stations over 2 years to show that maximal low-level jet (LLJ) frequency occurs in the Oklahoma–Kansas region of the Great Plains and is dominant in summertime. A significant diurnal variation of geostrophic wind up to 6 m s^{-1} has been observed in this region,[13] which is caused by changes in thermal wind from the diurnal cycle of heating and cooling the sloping terrain and consequently the oscillation in the horizontal pressure gradient. Whiteman, Bian, and Zhong[10] collected data with a rawinsonde with eight launches per day around the ARM SGP site (36.601° N, 97.487° W) to investigate occurrences of LLJs and connections of LLJs in different seasons. Southerly LLJ wind speed maxima are most frequently found at 300–600 m AGL, and peak speeds, typically between 15 and 21 m s^{-1}, are attained at 02:00 central standard (local) time. The northerly jets are generally associated with cold-air outbreaks and are found in the cold air behind southward-moving cold fronts.

The wind turbine operates in the lower ∼100 m of the ABL; therefore, high-vertical-resolution data within the rotor layer every 10–30 min are of significant interest. The ARM has a 60-m meteorological (met) tower that has been collecting meteorological data since 2011. A scanning Doppler lidar[14] has provided profiles of wind speed and direction through the ABL since 2010. In this work, we use the long-term ARM observational data to characterize the wind shear and veer at the AWAKEN field campaign[1] site, which will facilitate our understanding of the site characteristics and eventually contribute to the design of the field campaign. This understanding will help us generate benchmark data for the simulation setup and numerical model validations. The AWAKEN field campaign focuses on selected wind plants close to the ARM SGP observatory to study the influence of the ABL on wind plants, and vice versa. The long-term observational data provided by the ARM SGP instruments are a great resource to investigate the atmospheric parameters that affect the wind plant performance.[15] We focus on wind shear and veer, which are quantities of primary interest for wind energy applications. The work has been divided into two main parts: (1) characterization of the wind shear and veer with scanning lidars, surface flux stations, and met tower data and (2) assessment of Monin–Obukhov similarity theory (MOST) to predict the wind shear under different atmospheric conditions.

II. SITE LOCATION AND INSTRUMENTS

Our analysis focuses on the targeted site for the AWAKEN field campaign: the DOE ARM SGP site in northern Oklahoma (Fig. 1). The site is heavily instrumented[16] and has been operational since 1989. The wide range of instruments deployed at the site provide an unprecedented array of observational data connected to different atmospheric processes relevant for ABL, aerosol modeling, cloud formation and precipitation, and wind energy applications.[17] A large number of wind plants have been built in the area surrounding the ARM SGP site in the last two decades. Considering the focus of this study and the availability of relevant wind speed measurements, we mostly concentrate on the observations collected at the ARM SGP

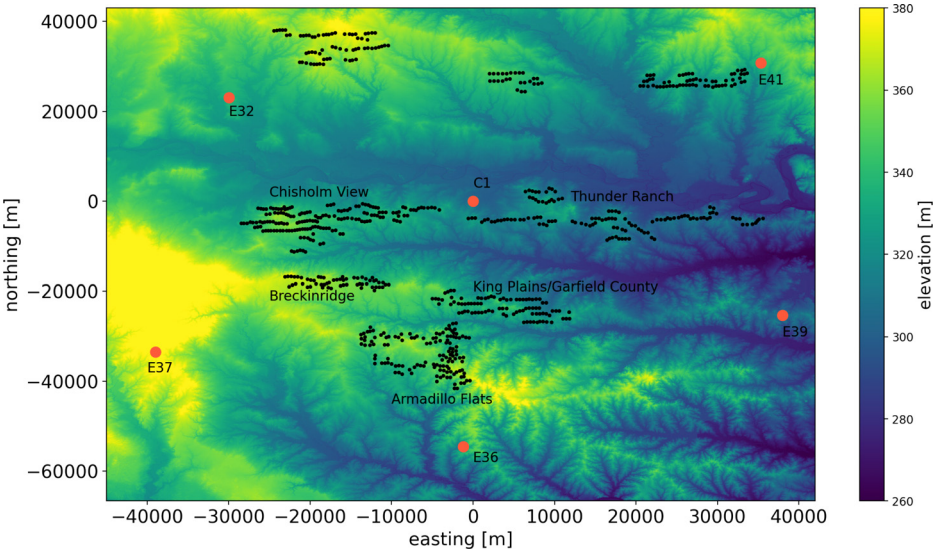

FIG. 1. Map of the test site for the AWAKEN field campaign. The black dots show the locations of the wind turbines in the region, and the red dots show a couple of important ARM measurement sites. Considering the availability of the data and type of instruments, only the measurements collected at the ARM site C1 are considered in this study.

central facility, referred to as the C1 site. At this location we use observations from a scanning Doppler lidar, a surface flux station, a 10-m-tall met tower, and a 60-m-tall met tower. The scanning Doppler lidar provides wind speed and wind direction up to ≈4 km AGL, starting from 91 m AGL, with a vertical resolution of approximately 26 m. The lidar performs 360° velocity azimuthal display scans with an elevation angle of 60° to provide vertical profiles of wind speed and direction. The details of the lidar scanning geometry and resolutions of the scans can be found in Newsom and Krishnamurthy.[14] Wind speed and wind direction data below 91 m AGL are taken from the neighboring met towers, which are within approximately 250 m of the Doppler lidar. The 60-m met tower provides wind speed, wind direction, and fluxes at 4, 25, and 60 m AGL, while the 10-m met tower provides wind speed and wind direction at 10 m AGL. Finally, the surface flux station provides high-frequency wind speed, pressure, temperature, and humidity data at 3 m AGL to retrieve the momentum and kinematic heat fluxes. For all instruments, we use observations from January 01, 2015, to December 31, 2020.

III. WIND RESOURCE CHARACTERIZATION

We focus on mean wind speed and direction in this section. Figure 2(a) shows a wind rose at 91 m AGL, which we use as a proxy hub height for the wind turbines in this area. The 6-year data show a predominant southerly wind flow at this site, with the wind flowing from 180° ± 10° approximately 40% of the time. The seasonal variability of the wind direction regimes is shown in Fig. 2(b). A clear seasonal cycle emerges: the winter season has wind coming from both the south and north, while summer has a higher frequency of wind coming from the south.

Given this strong connection between hub-height wind direction and season, we plot wind speed and direction at multiple heights as a function of time of day and month. Figure 3(a) shows the diurnal variability of the wind resource at SGP, whereas Fig. 3(b) shows the monthly variability over the course of the average year. In each panel, the contour color represents the wind speed, and arrows with quivers show the wind direction. The diurnal cycle in wind speed is much more evident than its annual variability. Nevertheless, the average wind speed at a given height is lower in summer months than in winter months. In the winter months, the predominant wind direction is from the south and north; in the summer months, the predominant wind direction is from the south. There is a west-to-east (e.g., clockwise) turning of the wind from lower heights to upper heights—the turning of the wind with height is termed wind veer. The wind veer at the site can be explained by the dominance of southerly wind and warm air advection from south to north, which causes thermal gradients at the site.

The mean wind direction at 91 m AGL is from the south and southeast at night and from the south and southwest during the day. There is a clear trend that the wind early in the night is from the southeast and turns clockwise after midnight. In the early morning, the wind direction is almost southerly. As the day progresses, the wind continues turning in a clockwise direction, and, by late afternoon, it comes from the southwest. However, the wind is mostly from the south in the evening before it turns counterclockwise at night to flow from the southeast again. In summary, the wind direction oscillates from the southwest to the southeast with the diurnal cycle. However, there is a clockwise turning of the wind with height that is dominant at night. This site is located in the northern hemisphere at latitude 36.601° N, and the impact of the Coriolis force on the wind direction with height and time of day is clearly observed. Unlike during daytime, the winds turn more clockwise direction with the shallow boundary layer and high wind speed [see contour in Fig. 3(a)] at nighttime. Similar to wind direction, wind speed also shows a distinct diurnal cycle. The wind speed close to the surface (e.g., 10 m) is lower at night compared to the wind speed during the day at the same height [Figs. 3(a) and 4(a)]. At upper heights (e.g., 91 m), the wind speed is higher at night than during the day at the same height. At a specific height, there is a clear oscillation of wind speed throughout the diurnal cycle, which can change the wind shear within the diurnal cycle. A clear visualization of the wind oscillation within the diurnal cycle is shown in Fig. 4. The mirrored variability of wind speed in Fig. 4(a) results in a clear variability in wind shear, which we quantify in terms of the power law exponent, α,

$$\alpha = \frac{log(U_2/U_1)}{log(z_2/z_1)}, \tag{1}$$

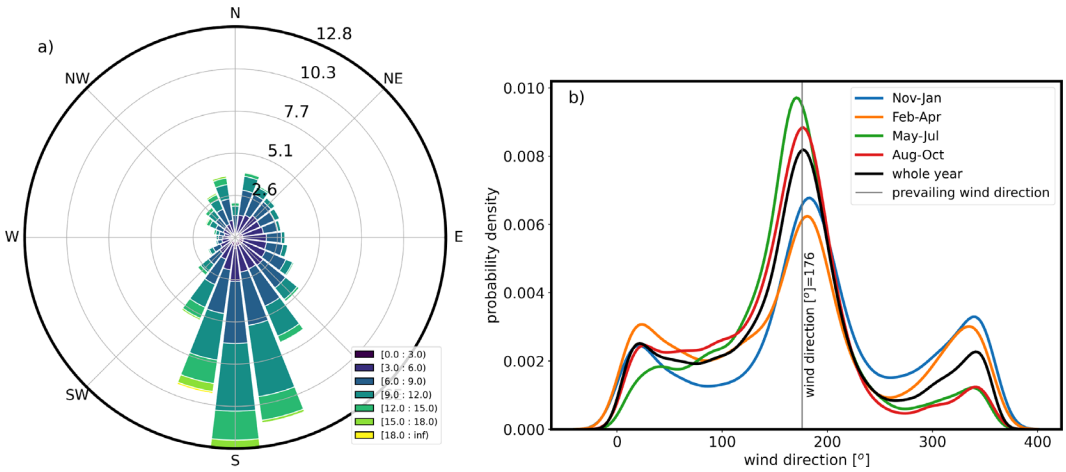

FIG. 2. Wind rose and prevailing wind direction at C1 location. (a) Wind rose at 91 m AGL. (b) Distribution of wind direction in different seasons at 91 m AGL.

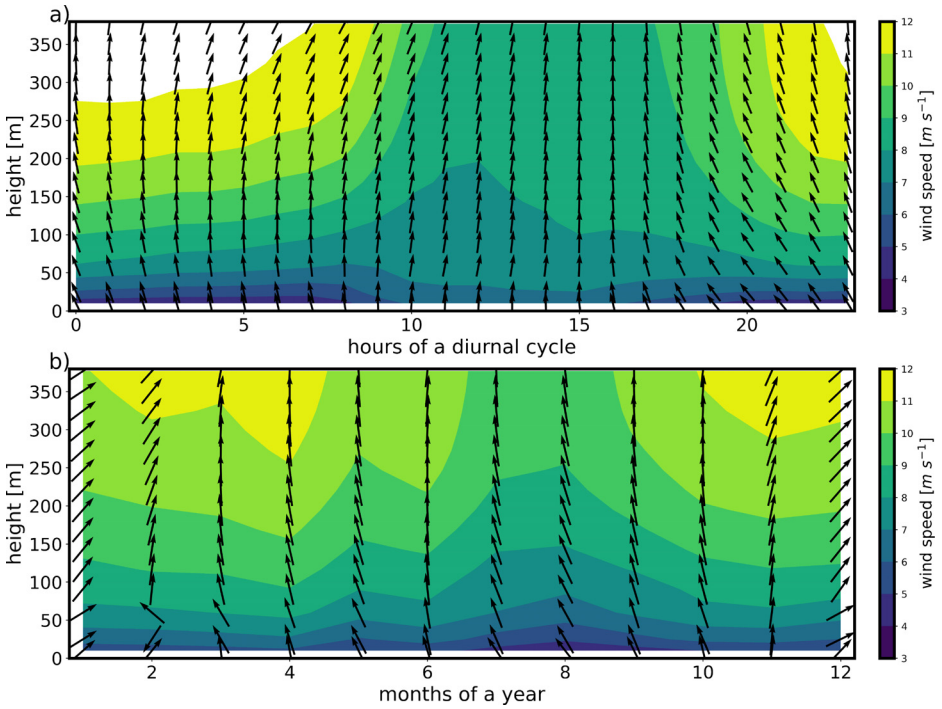

FIG. 3. Wind speed and direction for (a) different hours in a diurnal cycle (local time) and (b) different months in a year, where 01 means January and 12 means December. Note that wind direction is calculated with vector averaging of wind speed components.

where U_2 and U_1 are wind speeds at $z_2 = 169$ m and $z_1 = 10$ m. The power law exponent of wind speeds is refereed as wind shear exponent throughout the article. The wind shear is large at night and falls sharply in early morning. The lowest wind shears occur before midday. The wind shear starts to increase in the evening and reaches a maximum at midnight. The rise of wind shear in late evening is not as sharp as the drop of wind shear in early morning. Next, we consider the wind veer, β, defined as the change of wind direction per unit height between 10 and 169 m. The wind veer follows a pattern similar to the wind shear, but the wind veer is not as consistent as the wind shear at night [Fig. 4(b)].

A. Friction velocity and inertial oscillation

The surface stress changes over the diurnal cycle due to surface radiative cooling/heating and different forcings such as the time-dependent synoptic flow, the Coriolis force, and changes in the horizontal pressure gradient. The momentum is generally well-mixed during the day within the boundary layer, and the boundary layer can be extended up to a couple of kilometers. However, in the evening, the boundary layer depth collapses with a decrease in surface stress, which leads to an acceleration of wind near the surface due to the lower friction from the surface.[11,18] In other words, the oscillation of the ageostrophic wind triggered by the sudden decay of eddy viscosity after sunset reduces the frictional force closer to the surface, a mechanism described by Blackadar as frictional decoupling.[11] The inertial oscillation, which is a periodic fluctuation in the wind just above the surface of the earth, is dominated by the Coriolis and frictional forces.[8] There is a sudden increase in wind speed at 91 m AGL around 18:00 local time with a decrease in wind speed at 10 m AGL [Fig. 4(a)]. The drop in wind speed at 10 m AGL indicates that the height of the surface layer is dropping, and the increase in wind speed at 91 m AGL

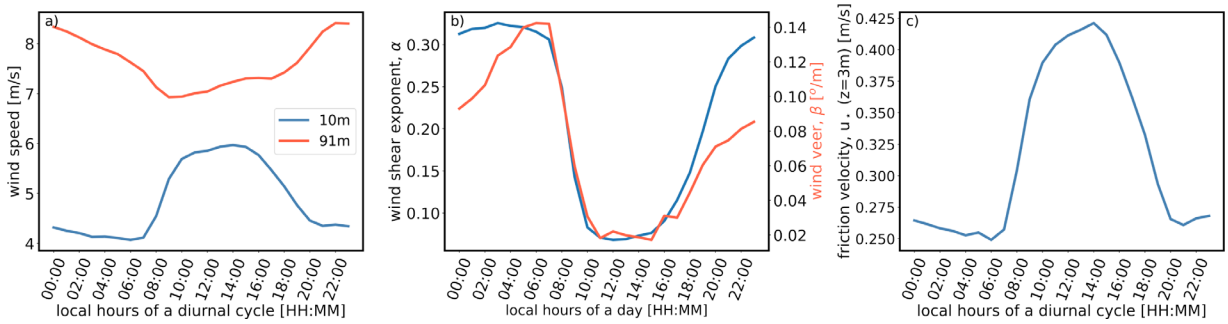

FIG. 4. Average diurnal cycle of (a) wind speed, (b) wind shear and veer, and (c) friction velocity. Wind shear and veer are calculated at heights between 10 and 169 m, and friction velocity is determined at 3 m AGL.

TABLE I. Obukhov length, L, at 3 m AGL.

	Unstable	Neutral	Stable
L^{-1} (m^{-1})	$-0.5 < L^{-1} < -0.002$	$-0.002 \leq L^{-1} \leq 0.002$	$0.002 < L^{-1} < 0.5$
Percentage (%)	48.1	4.7	47.2

indicates an acceleration of wind above the thin surface layer [Fig. 3(a)]. The inertial oscillation is directly connected to the friction velocity at 3 m AGL, as shown in Fig. 4(c). The friction velocity drops in the evening and continuously drops until 21:00 local time, while the wind speed at 91 m continuously increases until 22:00 local time before it becomes flat or starts to decrease. Zhong, Fast, and Bian[19] concluded that over the SGP, the inertial oscillation is more important than the pressure gradient related to cooling over the sloped terrain. Without investigating the impact of the sloped terrain in this study, it is clear that the inertial oscillations of the near-surface wind (e.g., 200 m) connected to the surface stress, or evening/morning transition, is important at the proposed AWAKEN site.

IV. ATMOSPHERIC STABILITY

This section investigates the impact of atmospheric stability on the observed wind shear and veer. The static atmospheric stability has been defined as a function of the Obukhov length, L, which defines the relative contribution of mechanical turbulence generated by the wind shear to the turbulence generated or suppressed by the buoyancy. The measurements needed for the Obukhov length calculation come from a flux station.[20] The met tower has a sonic anemometer along with pressure, humidity, and temperature sensors, all at a height of 3 m. The details about the measurements and calculation can be found in Cook.[20] The Obukhov length is determined by

$$L = -\frac{u_\star^3 T_v}{kg\overline{w'T_s'}}, \tag{2}$$

where $u_\star$ is friction velocity, k is the von Kármán constant, T_v is virtual temperature, and $\overline{w'T_s'}$ is the kinematic heat flux.

The atmospheric boundary layer is classified as unstable, neutral, and stable based on the range of the Obukhov length, as shown in Table I. The distribution of the inverse of the Obukhov length is presented in Fig. 6(b) to show the distribution of the atmospheric conditions. The weakly unstable and stable conditions dominate, where neutral condition occurs less than 5% (Table I) of the total time.

It has been shown that the diurnal cycle has a strong impact on wind speed and direction. The distribution of wind speed and direction with respect to the atmospheric stability were shown in Fig. 5 before presenting the wind shear and veer. The dominant wind direction in an unstable ABL is from the south and southwest, whereas the dominant wind direction in a stable ABL is from the south and southeast.

Figure 6(a) shows the wind shear distribution, which is bimodal, with peaks of the wind shear exponent, α, at 0.09 and 0.31. Because of this bimodal distribution, we investigate the connection of wind shear to atmospheric conditions—particularly, atmospheric stability. The wind shear data are separated based on the unstable and stable atmospheric conditions (Fig. 7). The median wind shear exponent values are 0.0904 and 0.323 for the unstable and stable ABL conditions, respectively. It should be noted that the standard deviation of the wind shear exponent in the stable ABL is higher than that for the unstable ABL, which indicates that wind shear varies more in a stable ABL than in an unstable ABL. Following the wind shear exponent, wind veer is also higher in the stable ABL than in the unstable ABL. The median

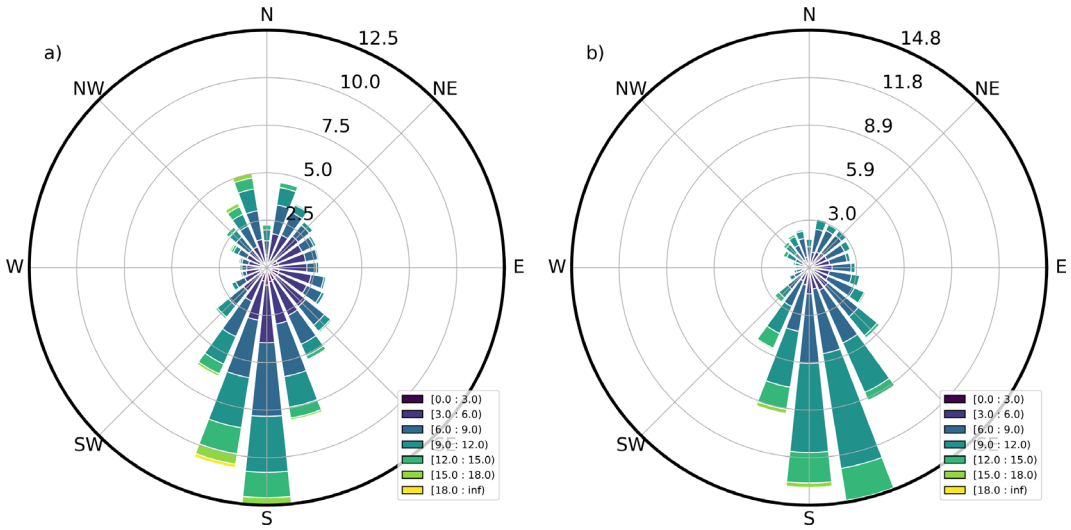

FIG. 5. Wind roses at 91 m AGL in (a) unstable and (b) stable atmospheric boundary layers.

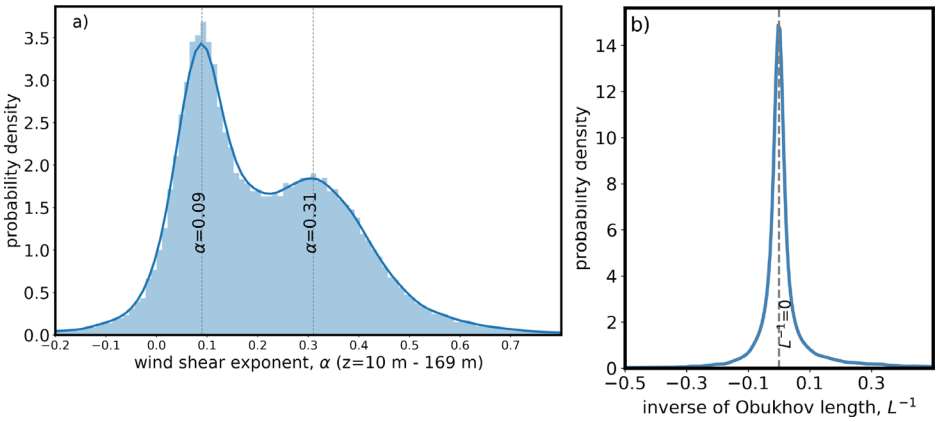

FIG. 6. Distribution of (a) wind shear exponent at the C1 location and (b) the inverse of the Obukhov length, L, at site C1.

wind veer values between 10 and 169 m AGL are 18° and 5.5° in stable and unstable ABLs, respectively. Due to the large wind veer in a stable ABL, which has occurrence of 47.2%, the top and bottom tips of the wind turbine blades at this site will face a large variation in wind direction. The hypothetical wind turbine, hub height of 91 m and rotor diameter of 127 m, considered in this study is based on the existing wind turbines in the area. The large variation of wind direction with height will contribute more to the turbine load, and the wakes from the turbines will propagate in different mean wind directions at different heights.[21] This spatially extended wake will reduce the power of downstream turbines and increase the load on the turbines. Because wind turbines are controlled based on the hub-height wind direction, the control strategy will suffer due to the extended wake directions with varying heights.

V. LOW-LEVEL JETS

A preliminary step in the analysis of LLJs is identifying the wind conditions that define the occurrence of such events. In this context, a profile is classified as an LLJ if it meets the following requisites:

(1) The height of maximum wind speed is between the second (60 m) and second-to-last (380 m) measurement height,

$$60 \leq z(U_{\max}) \leq 380\,\mathrm{m}.$$

(2) The wind speed drop-off above the jet nose meets minimum requirements in terms of dimensional and dimensionless threshold values,

$$\Delta U_{\mathrm{drop}} \geq 2\mathrm{ms}^{-1} \quad \text{and} \quad \frac{\Delta U_{\mathrm{drop}}}{U_{\mathrm{nose}}} \geq 10\%, \tag{3}$$

where $\Delta U_{\mathrm{drop}} = U_{\mathrm{top}} - U_{\mathrm{nose}}$, U_{nose} is wind speed at the nose, and U_{top} marks the wind speed at the top of the jet and is the first local minimum in wind speed identified above the nose. If a minimum is not found, a jet nose cannot be identified and the profile is not flagged as an LLJ. Depending on the threshold of the wind speed drop, ΔU_{drop}, the number of the detected events can vary.[22] Following Kalverla *et al.*,[22] the threshold used for ΔU_{drop} is 2 m s^{-1}. The enforcement of both dimensional and non-dimensional wind speed drop-off criteria is based on previous works.[22–24]

The LLJ detection criteria detects a total of 7086 30-min average LLJ profiles over the 6 years of data [Fig. 8(a)]. The LLJ events with nose heights less than the upper blade tip heights are expected to cause significant nonhomogeneity of the wind profile within the rotor area and enhance fatigue cycles on the turbine blades. As the nose height plays a significant role in wind energy applications, LLJ profiles are separated based on this quantity. The most frequent nose heights are

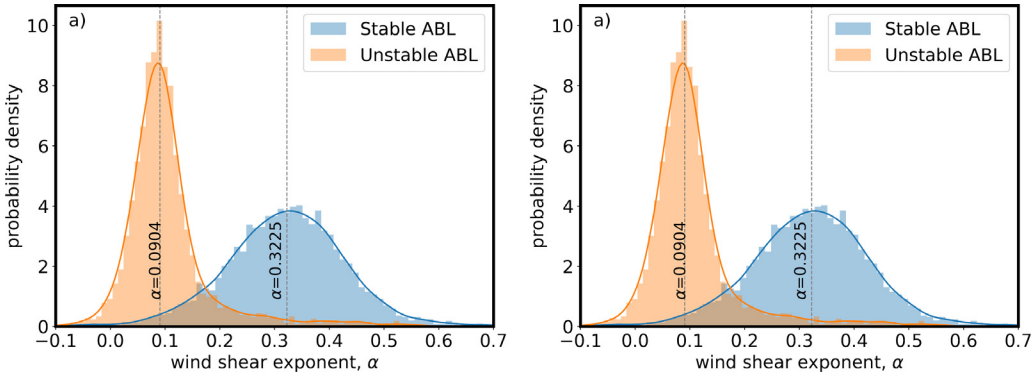

FIG. 7. Distributions of (a) wind shear exponent and (b) veer in unstable and stable atmospheric boundary layers.

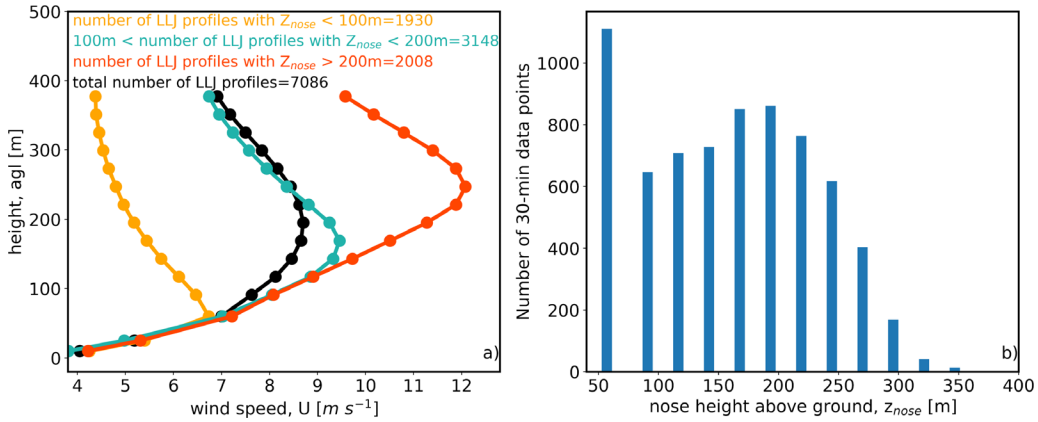

FIG. 8. (a) Mean wind speed profiles of the detected LLJs and (b) number of 30-min LLJ profiles as a function of the height of their nose.

60 and 190 m AGL [Fig. 8(b)], with an average nose height of 220 m AGL. However, LLJ profiles peaking at 60 m AGL correspond mostly to low wind speed events [Fig. 8(a)] and less shear. The percentage and absolute changes of wind speed criteria [Eq. (3) listed at the beginning of this section] used to identify the LLJ events can tag low wind speed events as LLJ cases [Fig. 8(a)]. The percentages of LLJ profiles that have nose heights less than 100 m and between 100 and 200 m are 29% and 45%, respectively, whereas higher altitude nose heights represent the remaining 28%. Remarkably, LLJ events with nose heights less than 200 m are quite frequent in this area.

Figure 9 reports the histograms of the wind speed at nose height, U_{nose}, differentiated based on the height of the nose itself according to the ranges defined earlier. If the nose height is within the rotor layer, the wind turbine blades face positive and negative wind speed gradients, a severely off-design condition that can add more load on the turbine blades, the gear boxes, and the bearings. The overall distribution of U_{nose} is positively skewed, with frequent extreme wind speed events (the 90th percentile is 18 m s^{-1}) and a median wind speed of 9.4 m s^{-1}. The LLJ events with high wind speed (e.g., 20 m s^{-1}) and lower nose heights can add significant loads to the wind turbines and need to be properly considered in the wind turbine blade design process.

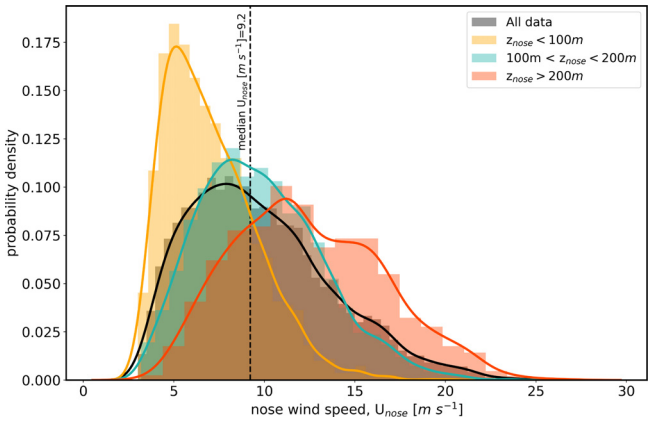

FIG. 9. Nose wind speed of the LLJ profiles and their probability of occurrence at different heights.

The connection among the LLJs, wind direction, shear exponent, and atmospheric stability is further investigated in Fig. 10. The distribution of wind shear exponent, α, for stable ABL and LLJ events is shown in Fig. 10(a). Wind shear exponent for the LLJ cases is defined in two different ways—between heights 10 and 169 m, $LLJ_{10m-169m}$ (similar to the stable cases), and between 10-m and nose heights, LLJ_{nose} [Fig. 10(a)], which showed negligible differences. For the wind shear exponent, α, calculated between heights 10 and 169 m, the stable ABL case peaks at $\alpha = 0.322$, and the distributions of the LLJ cases peak at $\alpha = 0.35$. The mean and median of the wind shear exponent are, respectively, 0.30 and 0.31 for the stable ABL case, and 0.34 and 0.35 for the LLJ cases. The LLJ cases have overall high wind shear compared to the stable ABL case. The distribution of the Obukhov length of both the stable ABL and LLJ cases is also shown in Fig. 10(b) to examine the corresponding stability conditions. The stable ABL case is defined according to Table I and always has a positive Obukhov length. However, the LLJ cases have both positive and negative Obukhov lengths [Fig. 10(b)] and have different stability distributions than the stable ABL case.

The LLJ cases are grouped into four categories based on the ranges of Obukhov length [Fig. 10(c)]. The LLJ cases that have negative Obukhov length (i.e., unstable conditions) are characterized by low wind shear (Fig. 12). A LLJ case that originates in a favorable condition can persist for a long time, and the transition phase before it disappears is also captured within the data. The weakly stable ABL case ($0 < L^{-1} \leq 0.05$) has a nose wind speed of 11.7 m s^{-1} compared to a nose wind speed of 8.5 m s^{-1} for the highly stable ABL case ($L^{-1} \geq 0.1$). The LLJs with high wind speed appear in weakly stable conditions. This is expected because strongly stable conditions defined based on the Obukhov length generally correspond to weak winds and strong net radiative cooling at the surface, whereas weakly stable cases are associated with strong winds and milder radiative cooling at the surface.[25] The characteristics of wind speed and shear for the LLJ cases at the AWAKEN site are aligned with the findings of Mahrt.[25]

Wind direction is critically connected to the formation of LLJs. Frictional decoupling influences the wind speed and surface stress, and wind speed magnitude is proportional to the Coriolis force, which

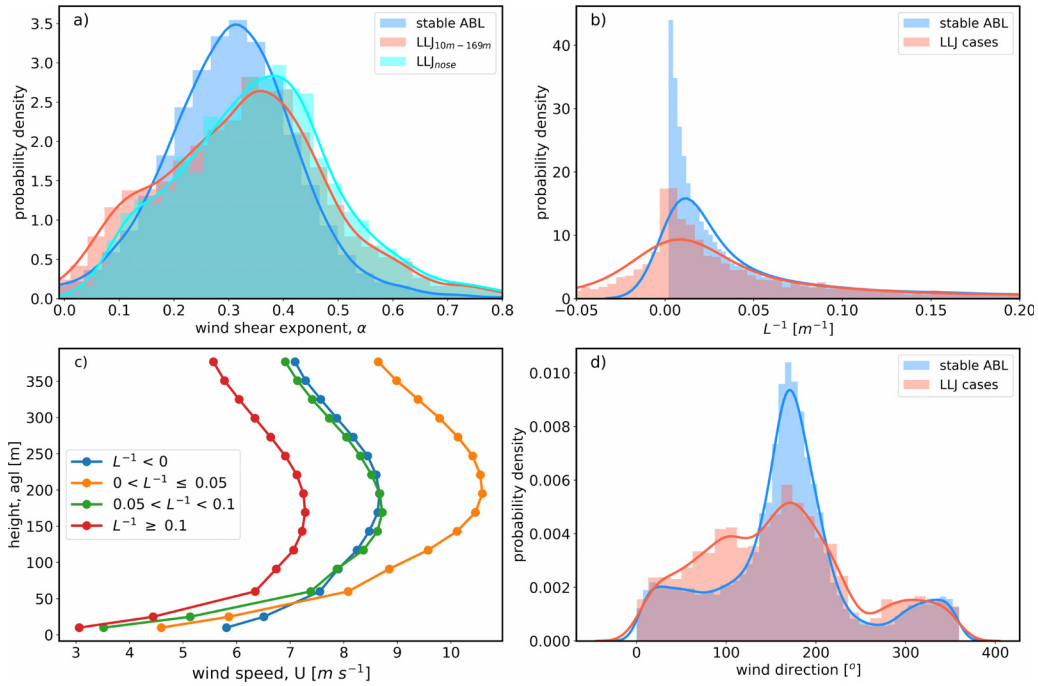

FIG. 10. Probability density of the LLJ profiles with (a) wind shear exponent. (b) Probability density of the LLJ profiles and stable ABL with the inverse of Obukhov length, *L*. (c) LLJ profiles under different stability regimes and (d) distribution of stable ABL and LLJ cases with wind direction.

ultimately impacts the wind direction. While the inertial oscillations resulting from the frictional decoupling in the lower atmosphere are a dominant mechanism for the occurrence of LLJs in summertime,[26] Holton[27] mentioned that the thermal effect can contribute significantly to the amplitude of the diurnal wind oscillation over sloping terrain. In the southern Great Plains, the gradual east-to-west terrain slope can create a horizontal temperature gradient on a daily basis,[10,28] which accelerates the thermal wind and LLJ initiation. Similarly, Hoxit[29] found that the thermal winds have a strong effect on the change in wind direction with height. The wind direction of the LLJs as a function of nose height are shown in Fig. 11. The stable ABL is dominant from the south and southeast wind directions, as mentioned earlier. However, the LLJ cases have more wind coming from the southeast or east compared to the stable or overall wind data [Figs. 10(c) and 11(a)]. For instance, stable cases have around 8% wind coming from the 90° ± 20° wind direction, while LLJ cases have 13% wind coming from the 90° ± 20° wind direction. With the increase in nose height, southeasterly winds become more dominant [Fig. 11(b)]. The clockwise turning of the wind with height and the wind veer that turbines face in the LLJ cases is confirmed by the average veer profiles visualized in Fig. 11(b). Figure 11(c) summarizes the dominant influences of wind direction on LLJs; LLJs from the south are stronger than those from the north.

Finally, the seasonal and diurnal variability of the dynamics of LLJ events are examined in this work. The number of 30-min-

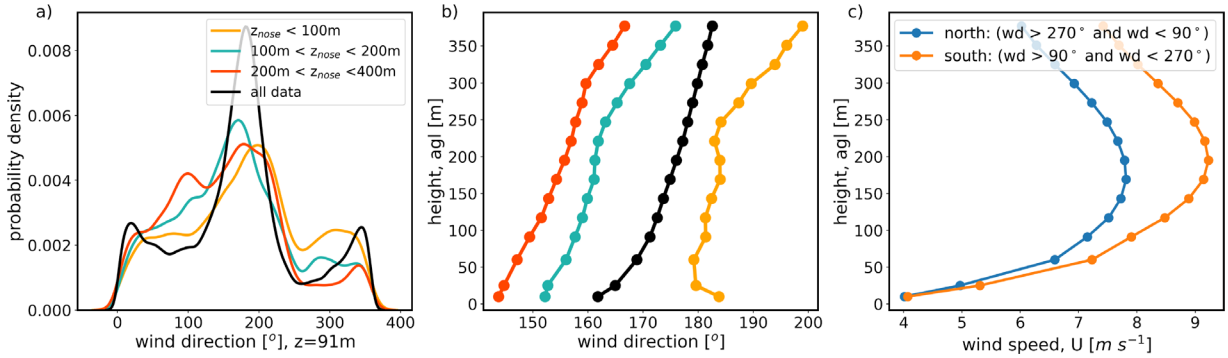

FIG. 11. (a) Probability density of nose heights with wind direction for the LLJ profiles. (b) Median wind direction profiles. (c) LLJ profiles from the north and south wind direction.

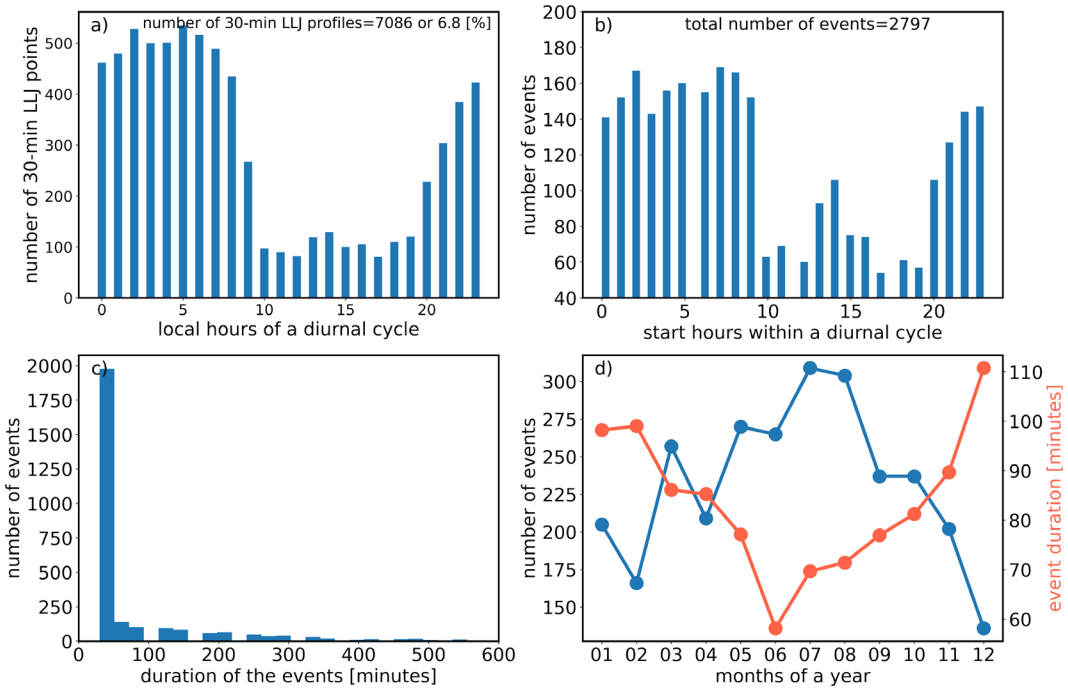

FIG. 12. Dynamics of LLJ events: (a) number of LLJ profiles with local hours of the diurnal cycle, (b) LLJ start hours within diurnal cycle, (c) overall histogram of LLJ duration, and (d) monthly distribution of LLJ events and event duration.

averaged LLJ data points is investigated with local hours and months of a year. It is clear that LLJ events occur mostly at night, starting in the evening (i.e., 20:00 local time) and dropping to a minimum in the late morning (i.e., 10:00) [Fig. 12(a)]. The number of LLJs is at a maximum in summer and at a minimum in winter. However, the number of discrete 30-min LLJ data points does not provide any information about the duration of the LLJ events. A long event will have more data points and a short event will have fewer data points. Depending on the seasons and atmospheric conditions, the durations of the LLJ events vary. Therefore, a single LLJ event is defined as all of the individual 30-min-averaged LLJ profiles that have gaps of less than 2 h. Temporal statistics of LLJ events are provided in Fig. 12(b). For a diurnal cycle, the number of events starts to increase after 20:00 local time and stays almost constant overnight, dropping after 10:00. Most of the events are short, and some events can persist more than 5 h. Interestingly, winter months have fewer LLJ events compared to summer months. However, LLJ events generated in summer months are usually shorter events, whereas LLJ events generated in winter months are longer events, particularly in November, December, January, and February.

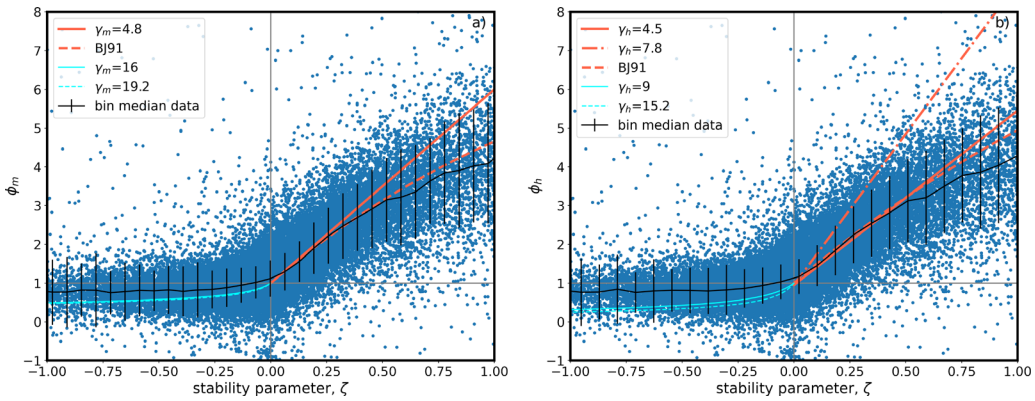

FIG. 13. (a) Non-dimensional wind shear and (b) non-dimensional temperature gradient.

VI. PREDICTION OF WIND SHEAR

A. Non-dimensional wind and temperature profiles

The analysis shows that wind shear and veer are well connected to atmospheric conditions; therefore, atmospheric conditions can be used to predict the wind shear and veer. Bodini and Optis[30,31] showed that machine learning can be successfully applied at the SGP site to extrapolate wind speed from near-surface data to hub height, and showed the limitations of conventional approaches. Nevertheless, numerical models predict wind shear based on the Monin–Obukhov similarity theory (MOST), so that it is still important to explore the capabilities of MOST by taking advantage of the long-term dataset and its analysis presented in this work. This section presents the prediction of wind shear using MOST and identifies the limitations of MOST in predicting wind shear using the available upper-height wind measurements.

The ARM site provides high-frequency wind speed and temperature data at multiple heights close to the surface. The high-frequency data are used to calculate the time-averaged turbulent parameters needed for the non-dimensional wind speed (ϕ_m) and temperature (ϕ_h) profiles within the surface layer (e.g., 10 m AGL). MOST implies a unique function depending on the non-dimensional stability parameter, z/L, which will be referred to as stability parameter, ζ,

$$\frac{kz}{u_\star}\frac{\delta U}{\delta z} = \phi_m(\zeta), \tag{4}$$

$$\frac{kz}{\theta_\star}\frac{\delta \theta}{\delta z} = \phi_h(\zeta), \tag{5}$$

where $k = 0.4$ is the von Kármán constant, $u_\star$ is the friction velocity, z is the height above ground, U is the time-averaged wind speed, θ is the time-averaged potential temperature, $\theta_\star$ is the temperature scale ($\theta_\star = Hs/\rho\, c_p\, u_\star$), H_s is the heat flux, ρ is the time-averaged density of air, c_p is the air-specific heat, and P_r is the turbulent Prandtl number. The turbulent Prandtl number is defined as the ratio between the momentum eddy diffusivity and the heat transfer eddy diffusivity.

The universal functions[32] are proposed to formulate non-dimensional wind and temperature profiles based on observational data. The commonly used universal functions are proposed by Businger[33] and Dyer.[34] For unstable conditions ($\zeta < 0$),

$$\phi_m(\zeta) = (1 - \gamma_m\zeta)^{-0.25}; \quad \phi_h(\zeta) = P_r(1 - \gamma_h\zeta)^{-0.5}. \tag{6}$$

For stable conditions ($\zeta > 0$),

$$\phi_m(\zeta) = (1 + \gamma_m\zeta); \quad \phi_h(\zeta) = (P_r + \gamma_h\zeta). \tag{7}$$

Equations (6) and (7) are proposed with $k = 0.37$ and $P_r = 0.74$ by Businger[33] based on the Kansas experimental data.[35] Later, the constants are modified to $k = 0.40$, $P_r = 1.0$ by Dyer,[34] and $k = 0.41$, $P_r = 0.95$ by Högström.[36] The universal functions and their formulations can be found in different sources,[36] but the process is shown to provide the background information needed before presenting the results,

$$\int_{U(z_1)}^{U(z_2)} \delta U = \int_{U(z_1)}^{U(z_2)} \frac{u_\star \phi_m}{kz}\delta z; \quad \int_{\theta(z_1)}^{\theta(z_2)} \delta\theta = \int_{\theta(z_1)}^{\theta(z_2)} \frac{\theta_\star \phi_h}{kz}\delta z. \tag{8}$$

Stability functions for wind and temperature are defined as

$$\Psi_m(\zeta) = \int_{\zeta_1}^{\zeta_2} \frac{1-\phi_m}{\zeta}\delta\zeta; \quad \Psi_h(\zeta) = \int_{\zeta_1}^{\zeta_2} \frac{1-\phi_h}{\zeta}\delta\zeta. \tag{9}$$

Solving equations from height z_1 to z_2 and using Eq. (9), we have

$$\begin{aligned} U(z_2) &= U(z_1) + \frac{u_\star}{k}[ln(z_2/z_1) - \Psi_m(\zeta_2) + \Psi_m(\zeta_1)];\\ \theta(z_2) &= \theta(z_1) + \frac{\theta_\star}{k}[ln(z_2/z_1) - \Psi_h(\zeta_2) + \Psi_h(\zeta_1)]. \end{aligned} \tag{10}$$

If we consider the first height z_1 as the surface roughness, z_0, then Eq. (10) transforms to

$$\begin{aligned} U(z) &= \frac{u_\star}{k}[ln(z/z_o) + \Psi_m(\zeta)];\\ \theta(z) &= \theta(z_o) + \frac{\theta_\star}{k}[ln(z/z_o) + \Psi_h(\zeta)]. \end{aligned} \tag{11}$$

Wind speed at upper heights can be extrapolated by

$$U(z_2) = U(z_1)\frac{[ln(z/z_o) + \Psi_m(\zeta_2)]}{[ln(z/z_o) + \Psi_m(\zeta_1)]}. \tag{12}$$

The wind speed can be extrapolated at upper heights by using both Eqs. (10) and (11). In addition to the stability functions, the formulation in Eq. (10) requires surface friction velocity, which is available from the surface flux stations, and the formulation in Eq. (10) requires surface roughness height, z_o. The surface roughness height, z_0, is calculated using the observational data in neutral ABL.

According to Paulson,[37] if we use Eqs. (7)–(9), we have

$$\Psi_m = log\left[\left(\frac{1+x^2}{2}\right)\left(\frac{1+x}{2}\right)^2\right] - 2\tan^{-1}x + \pi/2; \quad \Psi_h = -\gamma_m\zeta, \tag{13}$$

where $x = (1 - \gamma_m\zeta)^{0.25}$. The commonly used values for the constant γ_m are 15 (Businger[33]), 16 (Dyer[34] and Paulson[37]), 19.2 (Högström[36]), and 4.7 (Businger[33]) for the unstable ABL, and 4.8 (Beare *et al.*[38]), 5 (Dyer[34]), and 6 (Högström[36]) for the stable ABL. The linear non-dimensional wind shear functions work well for the weakly stable case. The constant γ_m varies from 4 to 6 in different studies;[33,34] the GABLS study[38] used 4.8. However, based on more observational data, it is shown that non-dimensional wind does not follow a linear trend in strong stable ABL regimes. Beljaars and Holtslag[39] (marked as BJ91 in this work) proposed nonlinear wind shear function based on the data collected at the Cabauw site,

$$\phi_m = 1 + \zeta\left[a + b\exp^{-d\zeta}(1 + c - d\zeta)\right], \tag{14}$$

where $a = 1$, $b = 0.667$, $c = 5$, and $d = 0.35$. According to Eq. (9), the stability function for stable conditions is

$$\Psi_m = -a\zeta - b(\zeta - c/d) * \exp^{(-d\zeta)} - bc/d, \tag{15}$$

where $a = 1$, $b = 0.667$, $c = 5$, and $d = 0.35$. The wind and temperature data at 3 and 10 m are considered to investigate the behavior of non-dimensional wind shear and temperature within the surface layer (Fig. 13). It is clear that the linear function works well for the weakly stable case but does not perform well after $\zeta = 0.3$. However, the nonlinear wind shear function proposed by Beljaars and Holtslag[39] works well for both weak and strongly stratified stable ABL cases. Similarly,

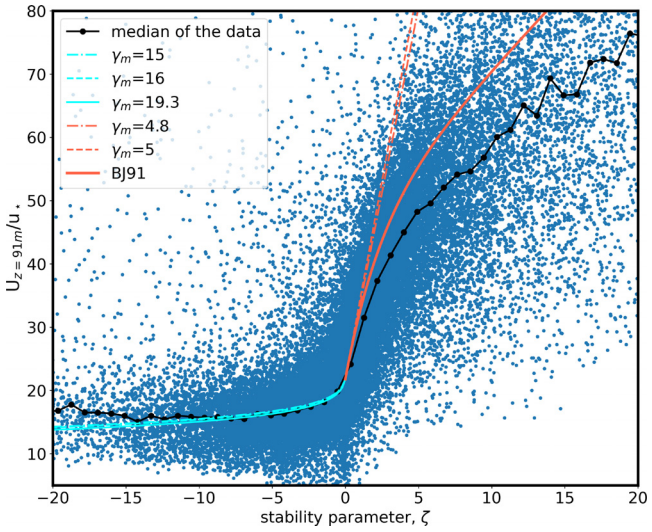

FIG. 14. Prediction of wind shear at 91 m AGL using wind speed measured at 10 m AGL.

the temperature wind shear function proposed by Beljaars and Holtslag[39] works well for the stable ABL. For the unstable ABL, the non-dimensional wind shear function is not much sensitive depending on the values of $\gamma_m = 16$ and $\gamma_m = 19.2$ proposed by Beljaars and Holtslag[39] and Dyer.[34] However, the non-dimensional temperature gradient for the unstable ABL at the site is noticeably different from the proposed functions by Högström,[36] Beljaars and Holtslag,[39] and Businger.[33]

B. Hub height wind speed prediction

The non-dimensional wind and temperature gradient data provide a good representation of the behavior of the site compared to the different non-dimensional and stability functions proposed using MOST. The surface layer relationships are applied to extrapolate the wind data from lower altitudes to upper altitudes. The target extrapolation height for wind speed is close to the hub height of the wind turbines in this area and the lowest height data available from the scanning lidar, which is 91 m AGL. The scanning lidar data at 91 m AGL will be benchmark data for the extrapolated wind speed data. The different stability functions are used to extrapolate the data at 10–91 m. A comparison between the extrapolated data and the lidar data are provided in Fig. 14. From different relations presented in this work, Eq. (13) with $\gamma_m = 16$ works well for the unstable ABL, whereas the nonlinear stability function [Eq. (14)] works better for the stable ABL.

The accuracy of extrapolation of wind speed using the selected stability functions is quantified in Fig. 15. The 6 years of wind data at 10 m AGL are extrapolated to 91 m AGL, and we conclude that extrapolating wind speed based on MOST works well for the unstable ABL at this site, whereas the extrapolation has more bias in the stable ABL (Fig. 15) than in the unstable ABL. The results show that the extrapolation has a mean bias and RMSE of −0.36 and 1.14 m s^{-1}, respectively, in the unstable ABL, whereas the stable ABL has a mean bias and RMSE of 0.65 and 1.95 m s^{-1}, respectively. The bias of the predicted wind speed in stable ABL has a dependency on the wind speed, and the bias drops with the increase in wind speed. The mean bias is 1.9 m s^{-1} for the bin of wind speed 5 m s^{-1}, whereas the mean bias is close to zero for the bin of wind speed 12 m s^{-1}. The low wind speed event could have negative shear, which can create significant bias in predicting the wind shear. All these values are significantly worse than what found when applying machine learning approaches,[30] which could represent a future replacement of some aspects of the MOST. The LLJ detection criteria show that many LLJ-like events have low wind speed and do not follow the power law. Therefore, the LLJ events are excluded from the stable ABL to evaluate the performance of the extrapolation of wind speed in stable ABL without any LLJ events. No significant change of bias and RMSE of the LLJ excluded stable cases is observed compared to the bias and RMSE of the stable ABL only. It warranted further investigations, but we leave this topic for future research.

VII. CONCLUSIONS

This study presented wind shear and veer characteristics at the AWAKEN field campaign site using 6 years of observational data collected by different instruments, including a scanning lidar, a met tower, a surface flux station, and a met station. Wind shear and veer in

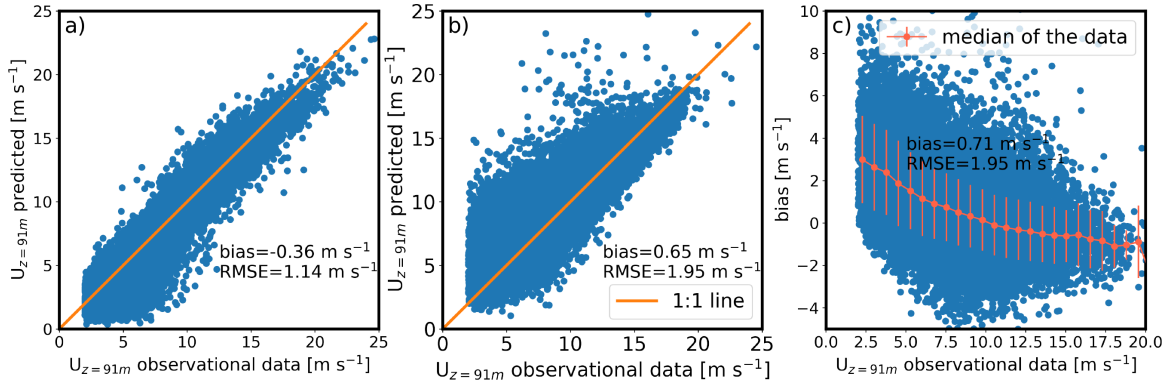

FIG. 15. Evaluations of wind shear prediction with the Monin–Obukhov similarity theory at 91 m AGL in (a) unstable ABL and (b) stable ABL. (c) The bias of the predicted wind speed in stable ABL. The orange line represents the median of the bias with standard deviation.

this SGP area are dominantly influenced by diurnal and seasonal variability. Wind flows dominantly from the south in the summer and from the south or north in the winter. During the diurnal cycle, wind flows dominantly from the southeast at night and from the south or southwest during the daytime. The turning of the wind direction from west to east with height due to the Coriolis force is clearly observed.

Wind speed at a height of 60 m or higher increases after evening and drops after early morning, whereas wind speed at a height of 10 m increases after early morning and decreases after evening. There is an oscillation of wind speed with the diurnal cycle, which creates a variation of wind shear throughout the diurnal cycle. The wind shear is at a minimum at midday and at a maximum near midnight, and it is inversely connected to the surface friction velocity observed at a height of 3 m. By observing the connection between the time of day and wind speed at the site, the influences of atmospheric stability on the wind shear and veer were examined. The wind is dominant from the southwest and southeast in unstably stratified ABL and stably stratified ABL, respectively. The bimodal distribution of the wind shear exponent, α, is connected to the stability of the ABL, where unstable ABL has a peak at 0.09, and stable ABL has a peak at 0.32.

Low-level jet events are an exception from the power law and cannot be represented only by the wind shear exponent. The LLJs at the site are identified and characterized to understand their properties. A total of 7086, 30-min averaged LLJs within 400 m of height are identified from the 6 years of data. The most frequent LLJ height is close to 200 m, with a median nose wind speed of 9.5 m s^{-1}. The LLJ events have a dominant southeast wind direction, and the LLJs from the south are stronger than the LLJs coming from the north. The shear of the LLJs is also characterized with respect to the atmospheric stability. The stronger wind and high-shear LLJs occur in a weakly stably stratified ABL, whereas lower wind speed and low-shear events occur in a strongly stratified stable ABL. The wind speed and shear of the LLJs decrease with an increase in stability. The influences of the seasonal variability on the LLJs are also observed. The LLJs occur primarily in the summertime, but summertime LLJ events have a shorter duration than the wintertime LLJ events. In this work, wind speeds up to a height of 400 m are considered to identify the stronger LLJ events within the lower surface of the ABL (e.g., 300 m). Depending on the considered heights of wind speeds and the criteria, the number of LLJ events could change.

The characterized wind shear at the site is predicted using the measurements at heights of 3 and 10 m based on the Monin–Obukhov similarity theory. Wind speed at a height of 91 m is predicted both for the unstable and stable ABLs with mean biases of −0.36 and 0.65 m s^{-1}, respectively. The nonlinear stability functions proposed by Beljaars and Holtslag[39] performs better in a stable ABL. In a stable ABL, the bias of the predicted wind speed at a height of 91 m depends on the wind speed—the bias reduces with an increase in the wind speed magnitude.

ACKNOWLEDGMENTS

This work was authored in part by the National Renewable Energy Laboratory, operated by Alliance for Sustainable Energy, LLC, for the U.S. Department of Energy (DOE) under Contract No. DE-AC36–08GO28308. Funding was provided by the U.S. Department of Energy Office of Energy Efficiency and Renewable Energy Wind Energy Technologies Office. The views expressed in the article do not necessarily represent the views of the DOE or the U.S. Government. The U.S. Government retains and the publisher, by accepting the article for publication, acknowledges that the U.S. Government retains a nonexclusive, paid-up, irrevocable, worldwide license to publish or reproduce the published form of this work, or allow others to do so, for U.S. Government purposes. Pacific Northwest National Laboratory (PNNL) is operated by Battelle Memorial Institute for the U.S. Department of Energy under Contract No. DE-AC05-76RL01830.

AUTHOR DECLARATIONS

Conflict of Interest

The authors have no conflicts to disclose.

Author Contributions

Mithu Debnath: Conceptualization (equal); Data curation (equal); Formal analysis (equal); Investigation (equal); Methodology (equal); Validation (equal); Visualization (equal); Writing – original draft (equal); Writing – review & editing (equal). **Petra M. Klein:** Writing – review & editing (equal). **Patrick Moriarty:** Funding acquisition (equal). **Raghavendra Krishnamurthy:** Writing – review & editing (equal). **Nicola Bodini:** Writing – review & editing (equal). **Rob Newsom:** Data curation (equal); Writing – review & editing (equal). **Eliot Quon:** Writing – review & editing (equal). **Julie Lundquist:** Writing – review & editing (equal). **Stefano Letizia:** Writing – review & editing (equal). **Giacomo Valerio Iungo:** Writing – review & editing (equal).

DATA AVAILABILITY

The data that support the findings of this study are available from the corresponding author upon reasonable request.

REFERENCES

[1]P. Moriarty, N. Hamilton, M. Debnath, R. Fao, J. Roadman, J. van Dam, T. Herges, B. Isom, J. Lundquist, D. Maniaci, B. Naughton, W. Shaw, and S. Wharton, "American wake experiment (AWAKEN)," arXiv:10.2172/1659798 (2020).
[2]M. Debnath, A. K. Scholbrock, D. Zalkind, P. Moriarty, E. Simley, N. Hamilton, C. Ivanov, R. S. Arthur, R. Barthelmie, N. Bodini, A. Brewer, L. Goldberger, T. Herges, B. Hirth, G. V. Iungo, D. Jager, C. Kaul, P. Klein, R. Krishnamurthy, S. Letizia, J. K. Lundquist, D. Maniaci, R. Newsom, M. Pekour, S. C. Pryor, M. T. Ritsche, J. Roadman, J. Schroeder, W. J. Shaw, J. V. Dam, and S. Wharton, "Design of the American wake experiment (AWAKEN) field campaign," J. Phys.: Conf. Ser. **2265**, 022058 (2022).
[3]R. Wagner, M. Courtney, J. Gottschall, and P. Lindelöw-Marsden, "Accounting for the speed shear in wind turbine power performance measurement," Wind Energy **14**, 993–1004 (2011).
[4]A. Choukulkar, Y. Pichugina, C. T. M. Clack, R. Calhoun, R. Banta, A. Brewer, and M. Hardesty, "A new formulation for rotor equivalent wind speed for wind resource assessment and wind power forecasting," Wind Energy **19**, 1439–1452 (2016).
[5]M. Sanchez Gomez and J. K. Lundquist, "The effects of wind veer during the morning and evening transitions," J. Phys.: Conf. Ser. **1452**, 012075 (2020).
[6]P. Murphy, J. K. Lundquist, and P. Fleming, "How wind speed shear and directional veer affect the power production of a megawatt-scale operational wind turbine," Wind Energy Sci. **5**, 1169–1190 (2020).
[7]N. D. Kelley, B. J. Jonkman, and G. N. Scott, "Great plains turbulence environment: Its origins, impact, and simulation," paper presented at AWEA's 2006 WindPower Conference (2006).

[8]K. Walter, C. C. Weiss, A. H. P. Swift, J. Chapman, and N. D. Kelley, "Speed and direction shear in the stable nocturnal boundary layer," J. Sol. Energy Eng. **131**, 011013 (2009).
[9]A. Shapiro and E. Fedorovich, "Nocturnal low-level jet over a shallow slope," Acta Geophys. **57**, 950–980 (2009).
[10]C. D. Whiteman, X. Bian, and S. Zhong, "Low-level jet climatology from enhanced rawinsonde observations at a site in the southern Great Plains," J. Appl. Meteorol. **36**, 1363–1376 (1997).
[11]A. K. Blackadar, "Boundary layer wind maxima and their significance for the growth of nocturnal inversions," Bull. Am. Meteorol. Soc. **38**, 283–290 (1957).
[12]W. D. Bonner, "Climatology of the low level jet," Mon. Weather Rev. **96**, 833–850 (1968).
[13]R. T. McNider and R. A. Pielke, "Diurnal boundary-layer development over sloping terrain," J. Atmos. Sci. **38**, 2198–2212 (1981).
[14]R. Newsom and R. Krishnamurthy, "Doppler lidar (dl) instrument handbook," Technical Report No. DOE/SC-ARM/TR-101, 2020.
[15]N. Bodini, J. K. Lundquist, and P. Moriarty, "Wind plants can impact long-term local atmospheric conditions," Sci. Rep. **11**, 22939 (2021).
[16]D. L. Sisterson, R. A. Peppler, T. S. Cress, P. J. Lamb, and D. D. Turner, "The ARM Southern Great Plains (SGP) site," Meteorol. Monogr. **57**, 6.1–6.14 (2016).
[17]R. Krishnamurthy, R. K. Newsom, D. Chand, and W. J. Shaw, "Boundary layer climatology at arm southern great plains," Report No. PNNL-30832, 2021.
[18]L. Mahrt, "Stratified atmospheric boundary layers," Boundary Layer Meteorol. **90**, 375–396 (1999).
[19]S. Zhong, J. D. Fast, and X. Bian, "A case study of the great plains low-level jet using wind profiler network data and a high-resolution mesoscale model," Mon. Weather Rev. **124**, 785–806 (1996).
[20]D. R. Cook, "Eddy correlation flux measurement system (ECOR) instrument handbook," Report No. DOE/SC-ARM-TR-052, 2018.
[21]M. Abkar and F. Porté-Agel, "Influence of atmospheric stability on wind-turbine wakes: A large-eddy simulation study," Phys. Fluids **27**, 035104 (2015).
[22]P. C. Kalverla, J. B. Duncan, G. J. Steeneveld, and A. A. Holtslag, "Low-level jets over the North Sea based on ERA5 and observations: Together they do better," Wind Energy Sci. **4**, 193–209 (2019).
[23]P. Baas, F. C. Bosveld, H. Klein Baltink, and A. A. M. Holtslag, "A climatology of nocturnal low-level jets at Cabauw," J. Appl. Meteorol. Climatol. **48**, 1627–1642 (2009).
[24]M. Debnath, P. Doubrawa, M. Optis, P. Hawbecker, and N. Bodini, "Extreme wind shear events in us offshore wind energy areas and the role of induced stratification," Wind Energy Sci. **6**, 1043–1059 (2021).
[25]L. Mahrt, "Nocturnal boundary-layer regimes," Boundary Layer Meteorol. **88**, 255–278 (1998).
[26]T. R. Parish, A. R. Rodi, and R. D. Clark, "A case study of the summertime Great Plains low level jet," Mon. Weather Rev. **116**, 94–105 (1988).
[27]J. R. Holton, "The diurnal boundary layer wind oscillation above sloping terrain," Tellus **19**, 199–205 (1967).
[28]J. Song, K. Liao, R. L. Coulter, and B. M. Lesht, "Climatology of the low-level jet at the Southern Great Plains atmospheric boundary layer experiments site," J. Appl. Meteorol. **44**, 1593–1606 (2005).
[29]L. R. Hoxit, "Diurnal variations in planetary boundary-layer winds over land," Boundary Layer Meteorol. **8**, 21–38 (1975).
[30]N. Bodini and M. Optis, "The importance of round-robin validation when assessing machine-learning-based vertical extrapolation of wind speeds," Wind Energy Sci. **5**, 489–501 (2020).
[31]N. Bodini and M. Optis, "How accurate is a machine learning-based wind speed extrapolation under a round-robin approach?," J. Phys.: Conf. Ser. **1618**, 062037 (2020).
[32]E. K. Webb, "Profile relationships: The log-linear range, and extension to strong stability," Q. J. R. Meteorol. Soc. **96**, 67–90 (1970).
[33]J. A. Businger, J. C. Wyngaard, Y. Izumi, and E. F. Bradley, "Flux-profile relationship in the atmospheric surface layer," J. Atmos. Sci. **28**, 181–189 (1971).
[34]A. J. Dyer, "A review of flux-profile relationships," Boundary Layer Meteorol. **7**, 363–372 (1974).
[35]D. A. Haugen, J. C. Kaimal, and E. F. Bradley, "An experimental study of Reynolds stress and heat flux in the atmospheric surface layer," Q. J. R. Meteorol. Soc. **97**, 168–180 (1971).
[36]U. Högström, "Nondimensional wind and temperature profiles," Boundary Layer Meteorol. **42**, 55–78 (1988).
[37]C. A. Paulson, "The mathematical representation of wind speed and temperature profiles in the unstable atmospheric surface layer," J. Appl. Meteorol. Climatol. **9**, 857–861 (1970).
[38]R. J. Beare, M. K. Macvean, A. A. Holtslag, J. Cuxart, I. Esau, J. C. Golaz, M. A. Jimenez, M. Khairoutdinov, B. Kosovic, D. Lewellen, T. S. Lund, J. K. Lundquist, A. McCabe, A. F. Moene, Y. Noh, S. Raasch, and P. Sullivan, "An intercomparison of large-eddy simulations of the stable boundary layer," Boundary Layer Meteorol. **118**, 247–272 (2006).
[39]A. C. Beljaars and A. A. Holtslag, "Flux parameterization over land surfaces for atmospheric models," J. Appl. Meteorol. **30**, 327–341 (1991).